Chemical Science

ROYAL SOCIETY OF CHEMISTRY

EDGE ARTICLE

View Article Online
View Journal | View Issue

Cite this: *Chem. Sci.*, 2025, **16**, 20486

All publication charges for this article have been paid for by the Royal Society of Chemistry

Received 5th June 2025
Accepted 29th September 2025

DOI: 10.1039/d5sc04085j

rsc.li/chemical-science

Illumination-induced deep trap state activation at the nanocluster/TiO_2 interface: the origin of intrinsic photocapacitance in sensitized solar cells

Muhammad A. Abbas, †[a] Raju Thota,†[a] Minwook Jeon†[b] and Jin Ho Bang *[abc]

Noble metal nanoclusters (NCs) in photoelectrochemical systems reveal novel functionalities. This study unveils that metal nanocluster-sensitized solar cells (MCSSCs) can intrinsically function as photocapacitors, storing charge in the dark. Illumination of $Au_{22}(SG)_{18}$ NC-sensitized TiO_2 activates deep surface trap states, forming an interfacial capacitance responsible for a persistent dark built-in potential. Open-circuit voltage decay experiments demonstrate a stable dark voltage post-illumination, a phenomenon absent in applied-bias voltage decay experiments, highlighting the crucial role of photogenerated holes within NCs in charging this capacitor. A proposed model features TiO_2 deep traps as the negative electrode, glutathione ligands as the dielectric, and the NC core (hosting holes) as the positive electrode. This intrinsic photocapacitive behavior, achieved without external storage components, is unprecedented in sensitized solar cells. These findings offer profound insights into NC/TiO_2 interfacial dynamics and suggest MCSSCs as candidates for integrated solar energy conversion and storage, paving the way for novel photocapacitor designs.

Introduction

Noble metal nanoclusters (NCs), a subclass of metal nanoparticles in the nanoscale range consisting of only a few metallic atoms, exhibit promising properties for photoelectrochemical (PEC) applications.[1–4] Initially introduced as alternative sensitizers to dyes and quantum dots, NCs have the potential to broaden the absorption spectrum of wide-bandgap oxide semiconductors (*e.g.*, TiO_2) in PEC applications.[5–10] However, subsequent studies on NC-sensitized TiO_2 (NC-TiO_2) systems have unveiled distinct interfacial properties that differentiate them from dye- and quantum dot-sensitized counterparts.[11] For instance, unlike traditional sensitized solar cells, NC-based solar cells (*i.e.*, metal nanocluster-sensitized solar cells (MCSSCs)) are susceptible to severe hysteresis.[12] However, the addition of alkali ions during the adsorption of NCs on TiO_2 can effectively mitigate this hysteresis and significantly enhance power conversion efficiency. In addition, the impact of photodegradation on NCs differs markedly from that on conventional sensitizers. When an NC-TiO_2 photoelectrode is exposed to illumination, NCs can transform into nanoparticles due to photodegradation. Yet, carefully controlling this undesirable phenomenon can be advantageous, as nanoparticles can boost PEC performance through the plasmonic field effect.[13,14] Moreover, beyond their role as sensitizers, NCs can also function as co-catalysts in PEC applications.[15–17] Our recent research has demonstrated that the charge transfer mechanism at NC-TiO_2 photoelectrodes varies depending on the size of the NCs and the hole-scavenging capability of the electrolyte.[18–20] These diverse and unique PEC behaviors of NC-TiO_2 photoelectrodes highlight the necessity for further investigation to comprehensively understand their intricate properties and optimize their applications.

Despite extensive recent research, the repertoire of intriguing PEC behaviors exhibited by the NC-TiO_2 system continues to expand. In this study, we demonstrated a novel PEC phenomenon: illumination of MCSSCs activates deep surface trap states on TiO_2, forming a surface capacitor capable of storing charge for extended periods in the dark. This dark charge storage contributes to a residual dark voltage within the device, suggesting the potential of MCSSCs as a photocapacitor. Given that conventional solar cells cannot retain photogenerated charges in the dark,[21,22] this discovery is intriguing and significant. To date, most photosensitizer-based photocapacitors have relied on coupling a solar cell with a discrete supercapacitor unit.[21,23] For instance, a three-electrode device comprising a dye-sensitized TiO_2 photoanode and two carbon-coated capacitor electrodes achieved an energy density approximately five times greater than that of its two-electrode

[a]*Nanosensor Research Institute, Hanyang University ERICA, 55 Hanyangdaehak-ro, Sangnok-gu, Ansan, Gyeonggi-do 15588, Republic of Korea. E-mail: jbang@hanyang.ac.kr*

[b]*Department of Applied Chemistry, Center for Bionano Intelligence Education and Research, Hanyang University ERICA, 55 Hanyangdaehak-ro, Sangnok-gu, Ansan, Gyeonggi-do 15588, Republic of Korea*

[c]*Department of Energy and Bio Sciences, Hanyang University ERICA, 55 Hanyangdaehak-ro, Sangnok-gu, Ansan, Gyeonggi-do 15588, Republic of Korea*

† These authors contributed equally to this work.

predecessors.[24] Similarly, integrating an N3-sensitized TiO_2 electrode with a polymer-film capacitor yielded a photo-charged voltage of 0.75 V and a discharged energy density of 21.3 μWh cm^{-2}.[25] While minimizing self-discharge can be achieved by removing oxidizing species—as shown in a system with only a Co(II)(py-pz)$_3$ reducing shuttle where 22.6% of the open-circuit voltage (V_{OC}) persisted for hours[22]—this strategy severely compromises dye regeneration and long-term cycling stability. In stark contrast to these approaches, the photo-induced capacitance we report is achieved without any modification to the standard solar cell architecture. This intrinsic charge storage is an unprecedented feature in any sensitized solar cell configuration. We propose a physical model to account for this exceptional behavior and explore its broader implications for the operational mechanism of MCSSCs.

Experimental

Chemicals and materials

The following chemicals and materials were procured from Merck: gold chloride ($HAuCl_4 \cdot 3H_2O$, ≥99.9% trace metal basis), L-reduced-glutathione (GSH, 98%), sodium hydroxide (NaOH, semiconductor grade, ≥99.99% trace metal basis), sodium borohydride ($NaBH_4$, 98.0%), 2-propanol (anhydrous, 99.5%), and ethylenediaminetetraacetic acid (EDTA). Acetonitrile (reagent grade) was obtained from Daejung Chemicals. Titanium tetrachloride ($TiCl_4$, 99%) and sodium chloride (NaCl, ≥99.5%) were purchased from Junsei Chemical Co., Ltd. Thermoplastic sealing films (DuPont Surlyn, 60 μm) and TiO_2 paste (Ti-nanoxide T/SP) for the fabrication of the mesoporous TiO_2 film were acquired from Solaronix. Electrolyte (EL-HPE) and TiO_2 paste (18NR-AO) used for preparing the scattering layer were purchased from Greatcell Solar. Fluorine-doped tin oxide (FTO) coated glass with a resistivity of 7 Ω sq^{-1} was obtained from Pilkington.

Synthesis of Au NCs

$Au_{22}(SG)_{18}$ NCs were synthesized following a previously reported $NaBH_4$ reduction procedure.[26] Briefly, an aqueous solution (230 mL) was prepared by combining 12.5 mL of 20 mM $HAuCl_4$ and 7.5 mL of 50 mM GSH. The pH of this solution was then adjusted to 12.0 using a 1 M NaOH solution, followed by the dropwise addition of 0.5 mL of 3.5 mM $NaBH_4$ to initiate the reaction. The reaction proceeded under vigorous stirring (600 rpm) for 30 min and was subsequently quenched by adjusting the pH to 2.5. The resulting solution was then stirred gently (150 rpm) for 6 h. To preferentially isolate $Au_{22}(SG)_{18}$ NCs, acetonitrile was added at a volume ratio of 1 : 3 (v/v), and the mixture was centrifuged at 7000 rpm for 5 min. The obtained precipitate was dried and then dispersed in 10 mL of deionized water, followed by the addition of 12 mL of isopropyl alcohol to induce precipitation. The resulting precipitate was separated by centrifugation at 7000 rpm, yielding highly purified $Au_{22}(SG)_{18}$ NCs. The UV-vis absorption spectrum and electrospray ionization mass spectrometry (ESI-MS) results of the synthesized $Au_{22}(SG)_{18}$ NCs are presented in Fig. S1.

Fabrication of NC-TiO_2 photoelectrodes and solar cells

FTO glass substrates were cleaned using a detergent solution, followed by rinsing with deionized water and a 1 : 1 : 1 solvent mixture of ethanol, methanol, and acetone. Subsequently, the substrates were treated with $TiCl_4$ at 70 °C for 30 min. A mesoporous TiO_2 layer was deposited, followed by a secondary TiO_2 layer designed for light scattering. The resulting films were then sintered at 550 °C in a box furnace (SH-FU-4MH, SH Scientific, Co., Ltd) and subsequently subjected to a second $TiCl_4$ treatment. The resulting TiO_2 films exhibited a mixed-phase composition, with an anatase-to-rutile mass ratio of approximately 3 : 1 and a band gap of 3.16 eV (Fig. S2). For sensitization, the electrodes (active area: 0.188 cm^2) were immersed in the $Au_{22}(SG)_{18}$ NC solution, followed by rinsing with deionized water and ethanol. Meanwhile, platinum (Pt) counter electrodes were prepared by sputtering Pt onto FTO glass. Finally, solar cell devices were assembled using the NC-TiO_2 electrodes, an I^-/I_3^- redox mediator (Electrolyte EL-HPE, Dyesol-Timo), and the Pt counter electrode. The power conversion efficiency (PCE) of $Au_{22}(SG)_{18}$ NC-sensitized MCSSCs was 2.70 ± 0.11%, with a short-circuit current density of 4.61 ± 0.11 mA cm^{-2}, a V_{OC} of 0.710 ± 0.034 V, and a fill factor of 0.832 ± 0.05 (Fig. S3 and Table S1).

Characterization

UV-vis absorption spectra were recorded using a UV-vis spectrophotometer (SCINCO S-3100). The chemical composition of the as-prepared $Au_{22}(SG)_{18}$ NCs was confirmed by ESI-MS using a 6230B Accurate Mass TOF LC/MS system with AJS (Agilent Technologies), operated in negative-ion mode with the following parameters: a flow rate of 3.0 μL min^{-1}, a capillary voltage of 4.0 kV, a capillary temperature of 200 °C, and an m/z range of 1000–20000. For mass spectrometry analysis, each sample (5 mg in 5 mL) was dissolved in a 1 : 1 (v/v) mixture of 0.1 M triethylammonium acetate buffer (in ultrapure water) and methanol, and directly introduced into the instrument. Transmission electron microscopy (TEM) images of TiO_2 films were obtained using a transmission electron microscope (Titan TM 80-300, FEI). Near-surface chemical compositions and oxidation states were investigated by X-ray photoelectron spectroscopy (XPS, AXIS NOVA, Shimadzu Kratos). The density of states measurements were performed using cyclic voltammetry (CV) in the dark with a potentiostat (Gamry REF600). Prior to CV, TiO_2 and NC-TiO_2 electrodes were held at 1.2 V *vs.* the reversible hydrogen electrode (RHE) for 100 s under 1 sun illumination to ensure complete oxidation of surface states, as previously reported,[13] followed by a negative potential scan. All photoelectrochemical measurements were converted to the RHE using the following equation:

$$V\ (vs.\ RHE) = V\ (vs.\ Ag/AgCl) + 0.197 + pH \times 0.059 \quad (1)$$

Open-circuit voltage decay (OCVD) and applied-bias voltage decay (ABVD) analysis

OCVD traces were measured using a source meter (Keithley 2400) while the devices were illuminated with a solar simulator

(HAL-320, Asahi Spectra) calibrated to AM 1.5 G conditions with a CS-20 standard diode (Asahi Spectra). For ABVD experiments, a potentiostat (Gamry REF600) was employed to apply bias excitation, and the resulting voltage decay trace was recorded using a source meter. Electron lifetimes were then calculated from the time derivatives of the V_{OC} decay in both OCVD and ABVD traces, according to the following equation:[27]

$$\tau_n = -\frac{k_B T}{q}\left(\frac{dV_{OC}}{dt}\right)^{-1} \quad (2)$$

where τ_n is the electron lifetime, k_B, is the Boltzmann constant, T is the temperature, and q is the elementary charge, respectively.

Results and discussion

The immobilization of $Au_{22}(SG)_{18}$ NCs onto the mesoporous TiO_2 surface was predicated on electrostatic interactions between the two components.[7,28,29] High-resolution transmission electron microscopy (HRTEM) imaging confirmed the uniform dispersion of $Au_{22}(SG)_{18}$ NCs across the TiO_2 substrate (Fig. S4). It was hypothesized that the adsorption of these NCs onto the TiO_2 surface would introduce additional surface trap states, thereby modulating charge transfer dynamics upon their activation. To investigate this phenomenon, CV was performed on both pristine TiO_2 and NC-TiO_2 electrodes. Prior to CV analysis, electrodes underwent an oxidative pretreatment at 1.2 V_{RHE} (V *vs.* RHE) for 100 s under 1 sun illumination to ensure the complete oxidation of pre-existing surface states. In the initial negative-going potential sweep, the NC-TiO_2 electrode exhibited a prominent cathodic peak centered at approximately 0.058 V_{RHE}. This feature was notably attenuated, being barely perceptible, in the CV profile of the pristine TiO_2 electrode (Fig. 1a). The appearance of this cathodic peak is attributed to the reductive filling of deep electron trap states that were vacated during the oxidative pretreatment. It is noteworthy that this peak was absent in the second and subsequent CV scans, providing strong evidence that its origin lies in the charging of surface states rather than a reversible faradaic redox process (Fig. S5). Further supporting this interpretation, the peak current demonstrated a linear relationship with the scan rate (Fig. 1b and S6), a characteristic hallmark of capacitive behavior associated with surface states.[30] In addition, the corresponding anodic scan displayed a broader peak, which is indicative of

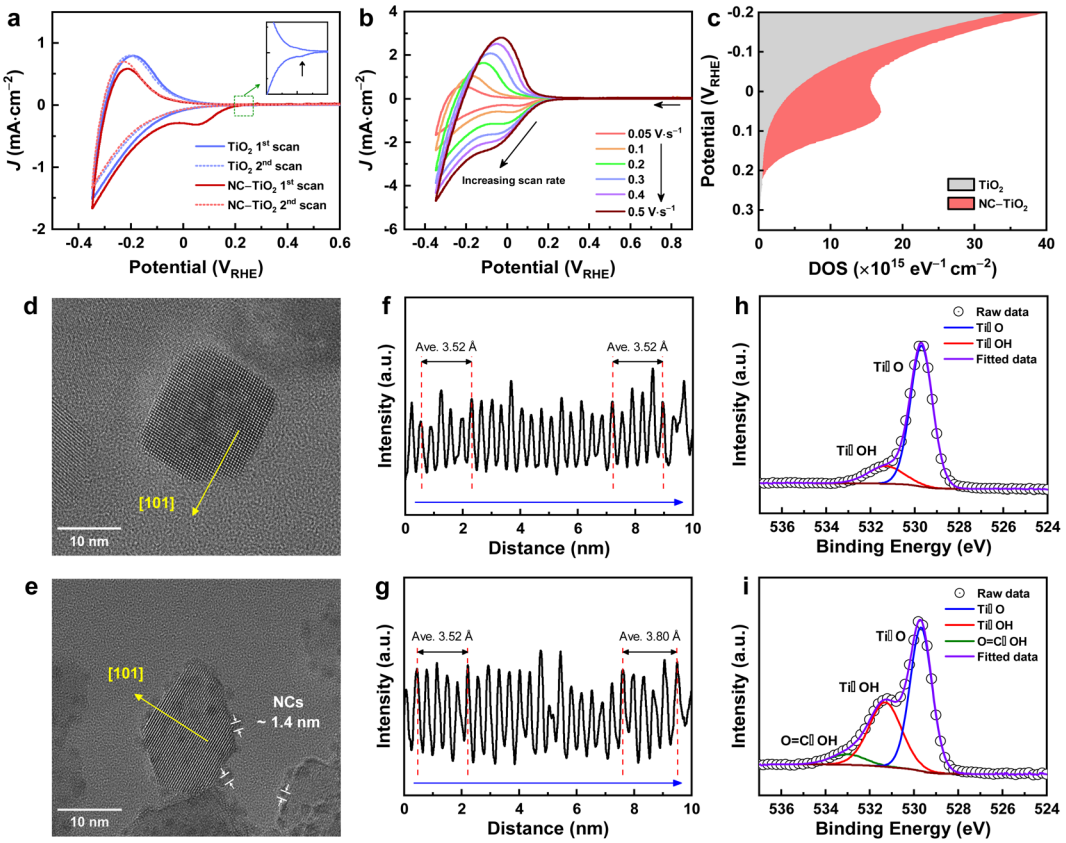

Fig. 1 (a) Cyclic voltammograms of pristine TiO_2 and NC-TiO_2 electrodes scanned at 0.05 V s^{-1} after applying a potential of 1.20 V_{RHE} for 100 s under 1 sun illumination in N_2-saturated 0.1 M ethylenediaminetetraacetic acid (aq). The inset highlights the capacitive peak observed in pristine TiO_2. (b) Scan rate-dependent cyclic voltammograms of NC-TiO_2. (c) DOS as a function of applied potential calculated from the cyclic voltammograms of TiO_2 and NC-TiO_2. HRTEM images displaying the (101) lattice plane of (d) pristine TiO_2 and (e) NC-TiO_2 and the corresponding lattice distance profiles along the [101] direction for (f) pristine TiO_2 and (g) NC-TiO_2, derived from images (d) and (e), respectively. The image in (e) shows NCs (~1.4 nm) anchored on the TiO_2 surface. XPS O 1s core-level spectra for (h) pristine TiO_2 and (i) NC-TiO_2.

sluggish electron detrapping kinetics from these deep trap states.[31] To further quantify the impact of NC functionalization on the electronic properties of TiO_2, the density of states (DOS) was derived from the CV measurements using the following relationship:[30]

$$\mathrm{DOS} = \frac{I}{ev} \quad (3)$$

where e is the elementary positive charge, v denotes the scan rate, and I represents the current measured at an applied potential. As presented in Fig. 1c, the NC-TiO_2 electrode exhibited a markedly higher DOS in comparison to the pristine TiO_2 electrode. Furthermore, this enhanced DOS was observed to be shifted towards more negative potentials, implying the formation of new trap state energy levels situated in closer proximity to the conduction band minimum of TiO_2.

To shed more light on the nature of surface trap states at the interface between NCs and TiO_2, a detailed analysis of the local crystal structures was performed. HRTEM images were acquired along the $[\bar{1}\bar{1}1]$ zone axis, an orientation confirmed by fast Fourier transform (FFT) analysis. This specific crystallographic orientation facilitated the unambiguous visualization of the (101) planes in both pristine TiO_2 and NC-TiO_2 samples (Fig. 1d and e). From the TEM intensity profiles, Ti–Ti interlayer distances (d-spacing) along the [101] direction were meticulously measured. Pristine TiO_2 exhibited a nearly consistent average d-spacing of 3.52 Å throughout its interior and exterior regions (Fig. 1f), which is indicative of its inherent structural integrity. In stark contrast, while the NC-TiO_2 sample maintained an interior d-spacing of 3.52 Å, its exterior layers, proximate to the NCs, revealed a significantly expanded average d-spacing of 3.80 Å (Fig. 1g and S7). This pronounced lattice expansion at the periphery of TiO_2 in the NC-TiO_2 electrode strongly suggests considerable structural distortion at the NC-TiO_2 interface.[32,33] Such interfacial distortion implies that the adsorption of NCs onto the TiO_2 surface induces a substantial population of surface defects, which are anticipated to manifest as electronic irregularities.[34] Further corroborating these surface modifications, XPS analysis revealed a markedly higher concentration of hydroxyl groups on the NC-TiO_2 surface compared to its pristine counterpart (Fig. 1h and i). Also, the O 1s XPS spectrum of NC-TiO_2 presented an additional peak centered at 533.1 eV, which is attributed to the GSH ligand capping the NCs. Peaks corresponding to lattice oxygen (Ti–O) and surface hydroxyl groups (Ti–OH) were identified at binding energies of 529.7 eV and 531.4 eV, respectively, in both samples, which is consistent with the established literature.[13,35,36] It is well-documented that surface hydroxyl groups on TiO_2 can function as surface trap states, mediating charge carrier recombination by simultaneously interacting with photogenerated electrons and holes.[37,38]

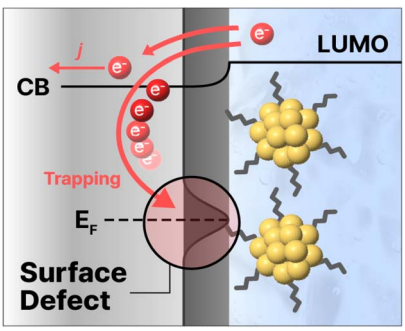

Fig. 2 Schematic illustration of surface trap states on TiO_2 induced by NC adsorption and subsequent electron trapping at these defects. The detailed band alignment at the NC-TiO_2 interface is provided in Fig. S8.

Critically, the deep trap states introduced by NC adsorption (Fig. 2) are posited to behave differently from the native trap states inherent to TiO_2, particularly upon photo-activation, as previously demonstrated.[18,20,39] We hypothesized that a higher density of these NC-induced deep trap states with slow detrapping kinetics could be strategically exploited for charge storage applications. Consequently, this work focuses on investigating the potential of these deep traps within the NC-TiO_2 system as a platform for photo-induced charging.

To elucidate the charge recombination dynamics at the NC-TiO_2 interface, OCVD studies were carried out. The solar cells, featuring the NC-TiO_2 photoelectrode, were initially illuminated under 1 sun conditions for a range of durations. Following this pre-illumination step, the subsequent decay of V_{OC} was recorded over 10 min, with the resulting data presented in Fig. 3a. The OCVD curves exhibited three distinct and notable features; firstly, V_{OC} decayed rapidly with an increase in light exposure duration; secondly, there were two distinct points on the OCVD curves where the rate of V_{OC} decay showed abrupt changes; lastly, V_{OC} decayed to a stable point very close to the thermal voltage after a 2 s light exposure (Fig. 3b). However, the rate of V_{OC} decay after 0.15 V slowed down dramatically with the increase in exposure time, and eventually, after 60 s of light exposure, V_{OC} seemed to become stable at 0.13 V, indicating the buildup of a stable dark voltage in the MCSSC. Since each of these points has interesting and important implications for NC-TiO_2 based PEC systems, we discuss the characteristics and implications of each point individually.

The V_{OC} decay was not characterized by a simple exponential decay but rather exhibited three distinct phases: V_{OC} to 0.47 V, 0.47 V to 0.15 V, and 0.15 V to near zero (Fig. 3b inset). The extracted electron lifetimes from the V_{OC} decay (Fig. 3c and d) clearly indicate the presence of two distinct energy states within the TiO_2 bandgap, located approximately 0.27 eV and 0.59 eV below the conduction band of TiO_2 (E_C), assuming that the quasi-Fermi level of TiO_2 (E_{Fn}) is very close to the E_C of TiO_2. These energy levels correspond to the surface states of TiO_2. While the shallow surface states at 0.27 eV below the conduction band (will hereafter be named E_{ss}) have previously been reported in NC-TiO_2 photoelectrodes,[13] the deep trap states at 0.59 eV below E_C (will be denoted as E_{sd}), to the best of our knowledge, are novel to the NC-TiO_2 system.

In addition, we observed a substantial increase in the rate of V_{OC} decay as the duration of light exposure lengthened. Following a 2 s light exposure, V_{OC} decayed to a stable state took over 200 s. In contrast, a 60 s exposure resulted in V_{OC} decay to a steady point within 75 s, with 90% of the decay occurring within the first 15 s (Fig. 3b). Typically, V_{OC} decay is attributed to

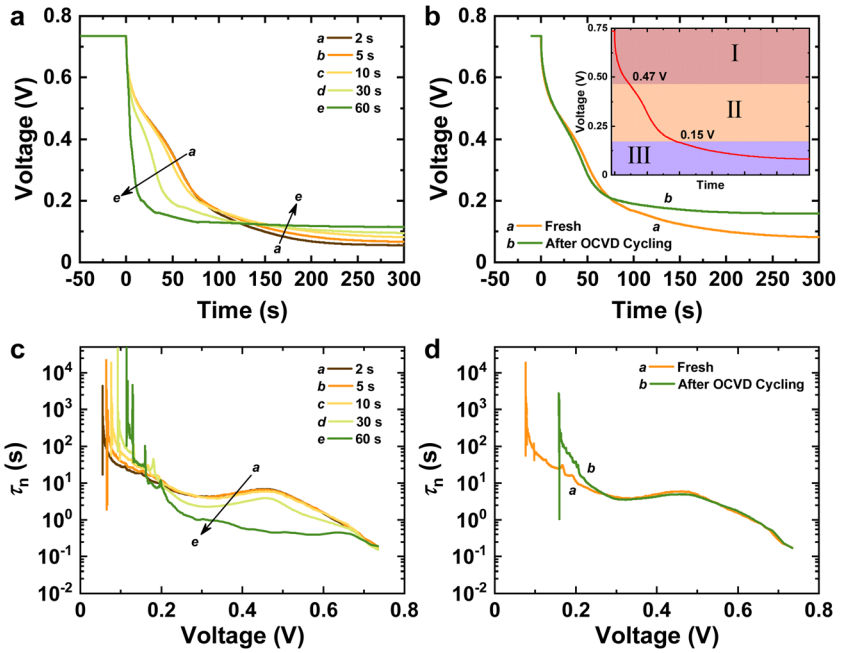

Fig. 3 (a) OCVD traces of $Au_{22}(SG)_{18}$ NC-sensitized MCSSCs following various light exposure durations. (b) OCVD traces before and after the OCVD experiment cycle. The inset of panel b illustrates the three distinct phases of V_{OC} decay. (c) Electron lifetimes (τ_n) extracted from the OCVD traces shown in panel a. (d) Electron lifetimes (τ_n) of OCVD traces before and after the OCVD experiment cycle.

the recombination of electrons from TiO_2 with either the electrolyte or the NCs at the TiO_2/NC/electrolyte interface. However, electrons may traverse multiple energy states prior to recombination. In general, two distinct recombination pathways can be identified: the recombination of electrons from TiO_2 with the electrolyte and the recombination of electrons from TiO_2 with holes within the NCs (Fig. S9a). Given that OCVD experiments require device excitation *via* illumination, which leads to the generation of electron–hole pairs within the NCs, both recombination pathways a and b become feasible (Fig. S9a). In contrast, ABVD experiments utilize applied bias excitation that does not produce any holes in the NCs, thereby precluding recombination *via* pathway a (Fig. S9b). Therefore, we carried out ABVD experiments as control experiments to elucidate the role of holes in the recombination process and to characterize the features of the V_{OC} decay curve. It is noteworthy that the validity of our comparative analysis was confirmed by the consistent Marcus–Gerischer kinetic parameters extracted from both OCVD and ABVD (Fig. S10 and Table S2), indicating an identical redox environment for both measurements.

The ABVD and OCVD curves exhibited comparable characteristics, except for a residual voltage buildup observed in the latter (Fig. 4a). Increasing the excitation time, whether through illumination or applied bias, accelerated the rate of voltage decay in both cases. ABVD experiments, conducted in the absence of light, precluded the formation of holes within the NCs. Despite this difference, both ABVD and OCVD experiments demonstrated a consistent increase in the rate of V_{OC} decay with prolonged excitation (Fig. 3a and 4a). Therefore, it can be inferred that the predominant pathway for electron recombination from TiO_2 involves direct interaction with the electrolyte (path b in Fig. S9). Another important observation was that prolonged excitation resulted in the activation of TiO_2 surface states and an increased recombination rate (Fig. 3b and 4b). Hence, TiO_2 surface states must have played a direct role in the recombination processes. Instead of the direct recombination of electrons from TiO_2 bulk states with the electrolyte, the recombination process may have occurred through the surface states.

The possible recombination pathways of electrons trapped on the TiO_2 surface with the electrolyte are depicted in Fig. 5a. Assuming no significant changes in the electrolyte behavior, paths 2, 3, and 4 may represent the dominant recombination paths; however, a single path may be dominant depending on the duration of the excitation signal. The electron lifetime of 2 s excitation OCVD traces shows a hump around 0.47 V (Fig. 3c and d). As this hump is a characteristic signal of the presence of shallow surface states,[40–42] path 2 may be the dominant recombination pathway. The presence of a hump at 0.47 V and a peak near 0.17 V (Fig. 3c) in 5 s to 30 s traces indicates that paths 2 and 3 might be active in the recombination processes. At 60 s of light excitation, however, no hump was observed at 0.47 V; therefore, path 4 may have been the most active. These observations indicate that NC-TiO_2 electrodes can have excitation duration-dependent recombination pathways. Such a rapid change in recombination paths is unprecedented in such systems and may have significant consequences for device performance but may also open avenues for new applications (*e.g.*, photocapacitors).

The most intriguing consequence of surface trap state activation at E_{sd} in the MCSSCs was the accumulation of a dark voltage. Following a 2 s light exposure, the V_{OC} decreased to

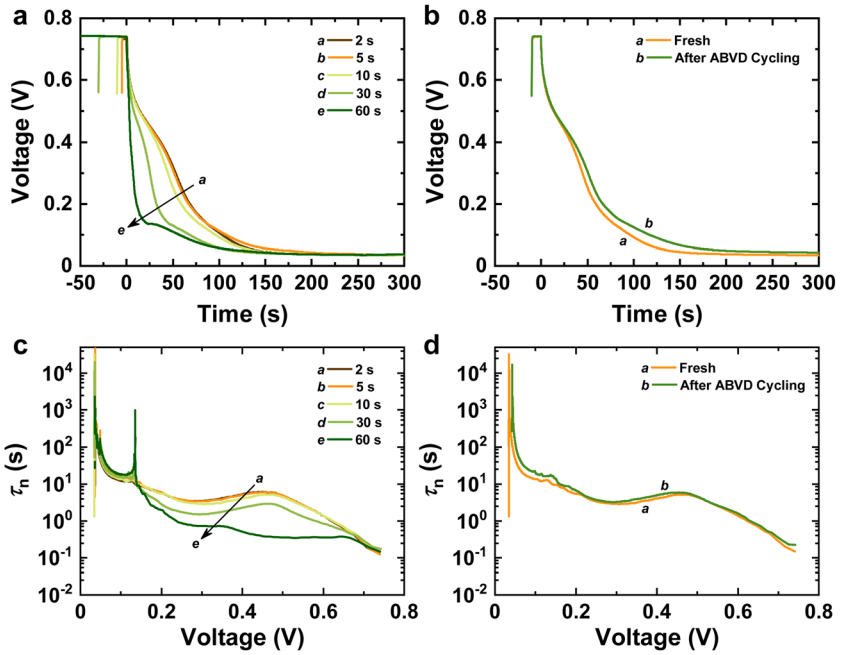

Fig. 4 (a) ABVD traces of $Au_{22}(SG)_{18}$ NC-sensitized MCSSCs following various light exposure durations. (b) ABVD curves before and after the ABVD experiment cycle. (c) Electron lifetimes (τ_n) extracted from the ABVD traces shown in panel a. (d) Electron lifetimes (τ_n) of ABVD traces before and after the ABVD experiment cycle.

a value of 56 mV, which is very close to the thermal voltage. However, a 10 s light exposure resulted in a V_{OC} decay to 83 mV after 5 min. Furthermore, after 60 s of light excitation, V_{OC} stabilized at 112 mV, exhibiting no significant change within the observed timeframe. Subsequent measurements of voltage decay curves following 2 s light excitation did not reverse the

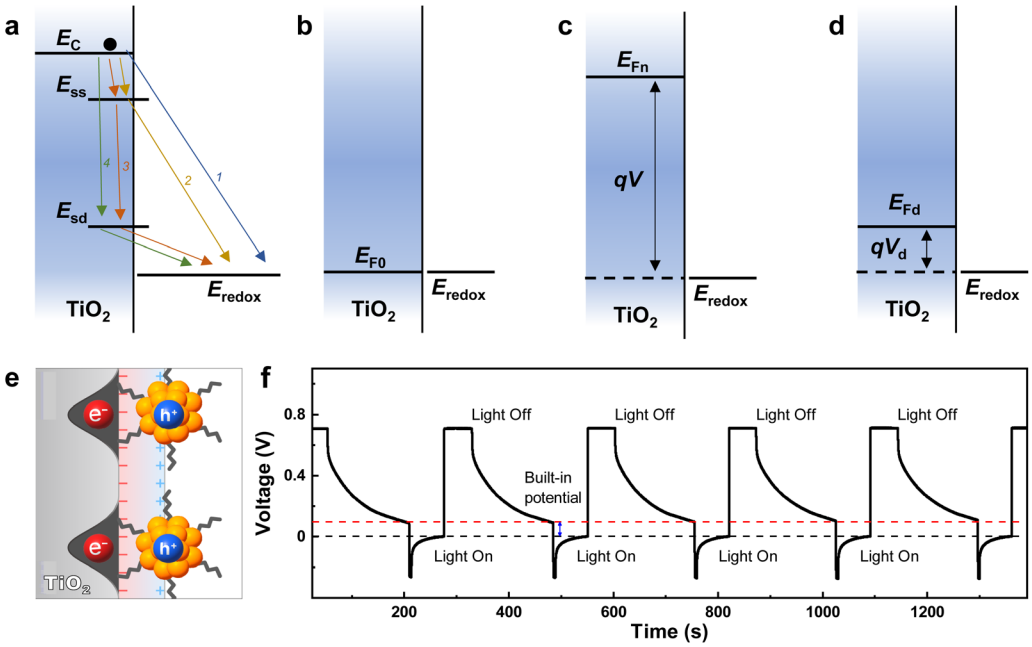

Fig. 5 (a) Possible electron recombination pathways of electrons with the electrolyte through various TiO_2 energy states. E_C is the TiO_2 conduction band position, E_{ss} is the TiO_2 shallow surface states, E_{sd} is the deep monoenergetic surface states, and E_{redox} is the electrolyte redox potential. For simplicity, electron detrapping paths are not shown. Energy positions of NC-TiO_2 and electrolyte (b) in the dark, (c) during illumination, and (d) after illumination. E_{F0} is the electron Fermi level in the dark, E_{Fn} is the electron quasi-Fermi level during illumination, E_{Fd} is the electron Fermi level after illumination, V_d is the residual voltage after illumination, and q is the elementary charge. (e) A surface capacitor model to explain the residual voltage in the MCSSC devices studied in the current work. (f) Photocapacitor voltage behavior after repeated charging and discharging cycles. Photocharging was performed under 1 sun (AM 1.5 G), and discharging in the dark was achieved by applying a 100 nA external load.

voltage buildup observed in the device (Fig. 3b). In addition, ABVD curves exhibited an increase in the voltage decay rate and activation of deep trap states, but no voltage buildup was observed during these experiments. Therefore, it can be concluded that the presence of NCs on the TiO_2 surface and light excitation are the two primary factors contributing to the residual voltage observed in the MCSSCs investigated in this study.

Under dark conditions, the E_{F0} is in equilibrium with the redox potential of the electrolyte (E_{redox}) (Fig. 5b). Upon photoexcitation of the NC-TiO_2 photoelectrode, electron–hole pairs are generated within the NCs, leading to electron transfer to TiO_2 and the formation of holes in the NCs. The accumulation of electrons in TiO_2 shifts its Fermi level upwards, away from equilibrium, to E_{Fn}. This difference between E_{redox} and E_{Fn} establishes a voltage within the device (Fig. 5c). Typically, at room temperature, a thermal voltage of 26 mV is present due to thermal excitation.[27] Consequently, when the light source is removed, the voltage gradually decays to this thermal value. In our experiments, however, photoexcitation of the MCSSC devices resulted in the generation of a significantly higher dark voltage of 112 mV.

The voltage (V) of an MCSSC device can be expressed using the following equation:[27,43]

$$qV = E_{Fn} - E_{redox} \quad (4)$$

where q is the elementary charge and E_{redox} is the redox potential of the electrolyte. The E_{redox} of the iodide/triiodide redox couple is given by[44]

$$E_{redox} = E_0^{'} + \frac{RT}{2F}\ln\left(\frac{[I_3^-]}{[I^-]^3}\right) \quad (5)$$

where $E_0^{'}$ is the equilibrium redox potential, and R, T, and F are the gas constant, temperature, and Faraday's constant, respectively. $[I_3^-]$ and $[I^-]$ represent the concentrations of triiodide and iodide species, respectively. While E_{redox} can be influenced by altering the $[I_3^-]/[I^-]^3$ ratio, the iodide/triiodide redox couple involves numerous redox species.[44] As a result, it is reasonable to assume that E_{redox} remains relatively constant. Even if an unforeseen reaction caused a change in E_{redox}, under dark conditions, electrons from TiO_2 recombine with the electrolyte, establishing an equilibrium. Therefore, the most likely explanation for the presence of V_{sd} is the stabilization of the Fermi level of TiO_2 near the E_{sd} surface states.

Despite the activation of E_{sd} states in both ABVD and OCVD experiments, the dark voltage was observed only in OCVD experiments. This suggests that specific parameters during the OCVD process stabilized the E_{Fn} of TiO_2 near E_{sd}, leading to dark voltage generation. Given that the sole mechanistic difference between ABVD and OCVD is the presence of holes in the NCs, it is plausible that the positive charge within the NCs contributed significantly to stabilizing the electron reservoir in TiO_2. Therefore, our results strongly indicate that the NC/GSH/TiO_2 combination forms a capacitor within the MCSSC, capable of storing sufficient charge to maintain the E_{Fn} of TiO_2 near the E_{sd} surface states under prolonged dark conditions (Fig. 5d). In our proposed model (Fig. 5e), the E_{sd} states developed on TiO_2 serve as the negative electrode, while the GSH ligands bound to the Au atoms in the NCs serve as the dielectric layer. The NC core acts as the positive electrode. The presence of holes in the NCs is essential for charge storage in this capacitor, as no charge accumulation was observed when an applied bias was used as the excitation source. Electrons stored within the capacitor help maintain the Fermi level of electrons in TiO_2 near E_{sd}, resulting in a dark voltage within the NC-TiO_2 device. Notably, this MCSSC-based photocapacitor demonstrated stable V_{OC} and dark built-in potential over repeated cycles of charging under 1 sun illumination and discharging in the dark (Fig. 5f). This photocapacitive behavior was quantified by analyzing the galvanostatic discharge curve shown in Fig. 5f. The areal capacitance was determined to be 0.266 ± 0.007 μF cm^{-2}. It is also noteworthy that this unique behavior is exclusive to the NC-TiO_2 system. Control experiments were carried out with TiO_2, GSH-sensitized TiO_2, and N719 dye-sensitized TiO_2 solar cell devices. However, none of the control devices exhibited any of the V_{OC} features observed in the MCSSC (Fig. 6). Moreover, no dependence on excitation duration was observed within the studied timeframes.

The rate of V_{OC} decay and the dark voltage of solar cell devices are typically influenced significantly by their temperature. While OCVD experiments can potentially elevate the device's temperature, careful measures were implemented to mitigate this effect. The observed increase in the V_{OC} decay rate during the OCVD experiments was also evident in the ABVD experiments, which are not susceptible to temperature

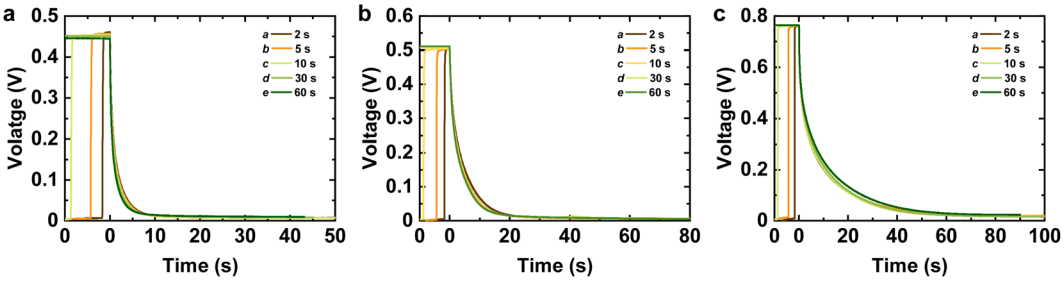

Fig. 6 OCVD traces of (a) TiO_2, (b) GSH-TiO_2, and (c) N719-TiO_2 solar cells with Pt as counter electrodes and the iodide/triiodide redox couple as electrolyte. Various light exposure durations (2, 5, 10, 30, and 60 s) were used for the OCVD experiments.

variations. Therefore, temperature fluctuations were not the primary cause of accelerated voltage decay with prolonged excitation. Moreover, if temperature variations were indeed responsible for the dark voltage observed in the OCVD experiments, a device temperature of 1290 K would have been necessary to produce a 112 mV voltage, which is calculated using the equation $V = k_bT/q$ (k_b is the Boltzmann constant, T is the absolute temperature and q is the elementary charge). Such a temperature is unattainable. Furthermore, the persistence of dark voltage even 10 min after light exposure, a sufficient time for the device to cool down, definitely rules out temperature fluctuations as the cause of the observed dark voltage buildup. On the other hand, the formation of a heterojunction between NCs and TiO_2 can result in Fermi level alignment,[13,45] which can lead to the storage of electrons in the NC-TiO_2 electrode and an upward shift in the Fermi level. This would create a built-in potential. However, no dark voltage was observed in the MCSSC, suggesting that the storage of holes in the NCs and electrons in TiO_2 is responsible for the dark voltage build-up in the MCSSC studied in this work. This exceptional behavior of NC-TiO_2 photoelectrodes suggests the intricate nature of their interfacial interactions. We envision that a deeper understanding of this phenomenon could not only enhance the efficiency of NC-based solar devices but also pave the way for the development of novel photocapacitor concepts.

Conclusions

We observed that illumination or applied bias of NC-sensitized solar cells activates two discrete energy levels within the TiO_2 surface states. These surface states directly facilitate recombination, resulting in a significant increase in the recombination rate with prolonged excitation. Most importantly, the deep trap states in conjunction with NCs can form a surface capacitor, generating a residual dark voltage within the device. However, this capacitor can only be charged through photoexcitation, while applied bias excitation fails to induce charging. As a result, the dark residual voltage was solely observable following photoexcitation of the device. In addition to highlighting the potential of MCSSCs as photocapacitors, we plan to explore the implications of this dark residual voltage on solar cell performance. Our ongoing research aims to further investigate the significance of this phenomenon in MCSSCs.

Author contributions

M. A. Abbas and J. H. Bang conceived and designed the experiments. M. A. Abbas, R. Thota, and M. Jeon carried out the experiments and analyzed the results. M. A. Abbas, M. Jeon, and J. H. Bang wrote the manuscript. All authors reviewed and approved the final manuscript.

Conflicts of interest

There are no conflicts to declare.

Data availability

The data supporting this article have been included as part of the supplementary information (SI). Supplementary information is available. See DOI: https://doi.org/10.1039/d5sc04085j.

Acknowledgements

This work was supported by grants from the Basic Science Research Program through the National Research Foundation (NRF) of Korea funded by the Ministry of Science and ICT (RS-2025-00557534) and by the Ministry of Education (NRF-2018R1A6A1A03024231).

Notes and references

1 M. A. Abbas, P. V. Kamat and J. H. Bang, *ACS Energy Lett.*, 2018, **3**, 840–854.
2 R. Jin, C. Zeng, M. Zhou and Y. Chen, *Chem. Rev.*, 2016, **116**, 10346–10413.
3 L. Chen, A. Black, W. J. Parak, C. Klinke and I. Chakraborty, *Aggregate*, 2022, **3**, e132.
4 Y. Liu, Y. Wang and N. Pinna, *ACS Mater. Lett.*, 2024, **6**, 2995–3006.
5 M. A. Abbas, T.-Y. Kim, S. U. Lee, Y. S. Kang and J. H. Bang, *J. Am. Chem. Soc.*, 2016, **138**, 390–401.
6 Y.-S. Chen, H. Choi and P. V. Kamat, *J. Am. Chem. Soc.*, 2013, **135**, 8822–8825.
7 Y.-S. Chen and P. V. Kamat, *J. Am. Chem. Soc.*, 2014, **136**, 6075–6082.
8 F.-X. Xiao, Z. Zeng and B. Liu, *J. Am. Chem. Soc.*, 2015, **137**, 10735–10744.
9 P. Su, B. Tang and F.-X. Xiao, *Small*, 2024, **20**, 2307619.
10 T. Chen, H. Lin, Y. Cao, Q. Yao and J. Xie, *Adv. Mater.*, 2022, **34**, 2103918.
11 M. A. Abbas, M. Jeon and J. H. Bang, *J. Phys. Chem. C*, 2022, **126**, 16928–16942.
12 M. A. Abbas, R. Thota, K. Pyo, D. Lee and J. H. Bang, *ACS Energy Lett.*, 2020, **5**, 1404–1406.
13 R. Khan, M. H. Naveen, M. A. Abbas, J. Lee, H. Kim and J. H. Bang, *ACS Energy Lett.*, 2021, **6**, 24–32.
14 M. A. Abbas, S. J. Yoon, R. Khan, J. Lee and J. H. Bang, *J. Phys. Chem. C*, 2019, **123**, 14921–14927.
15 W. Choi, G. Hu, K. Kwak, M. Kim, D.-e. Jiang, J.-P. Choi and D. Lee, *ACS Appl. Mater. Interfaces*, 2018, **10**, 44645–44653.
16 M. H. Naveen, R. Khan and J. H. Bang, *Chem. Mater.*, 2021, **33**, 7595–7612.
17 R. Jin, S. Zhao, C. Liu, M. Zhou, G. Panapitiya, Y. Xing, N. L. Rosi, J. P. Lewis and R. Jin, *Nanoscale*, 2017, **9**, 19183–19190.
18 M. A. Abbas and J. H. Bang, *ACS Appl. Mater. Interfaces*, 2022, **14**, 25409–25416.
19 M. A. Abbas and J. H. Bang, *ACS Energy Lett.*, 2020, **5**, 3718–3724.
20 S. Alam, M. Ali and J. H. Bang, *ACS Appl. Mater. Interfaces*, 2024, **16**, 30068–30076.

21 N. Flores-Diaz, F. De Rossi, A. Das, M. Deepa, F. Brunetti and M. Freitag, *Chem. Rev.*, 2023, **123**, 9327–9355.
22 Q. J. Yeow, C. Cuhadar, W. K. Tay, E. L. J. Tan, K. Johnson, S. E. Whang and H. N. Tsao, *ACS Appl. Energy Mater.*, 2022, **5**, 6746–6753.
23 T. Miyasaka and T. N. Murakami, *Appl. Phys. Lett.*, 2004, **85**, 3932–3934.
24 T. N. Murakami, N. Kawashima and T. Miyasaka, *Chem. Commun.*, 2005, 3346–3348.
25 C.-Y. Hsu, H.-W. Chen, K.-M. Lee, C.-W. Hu and K.-C. Ho, *J. Power Sources*, 2010, **195**, 6232–6238.
26 Y. Yu, Z. Luo, D. M. Chevrier, D. T. Leong, P. Zhang, D.-e. Jiang and J. Xie, *J. Am. Chem. Soc.*, 2014, **136**, 1246–1249.
27 A. Zaban, M. Greenshtein and J. Bisquert, *ChemPhysChem*, 2003, **4**, 859–864.
28 Y. Liu, E. Wierzbicka, A. Springer, N. Pinna and Y. Wang, *J. Phys. Chem. C*, 2022, **126**, 1778–1784.
29 I. Dolamic, C. Gautier, J. Boudon, N. Shalkevich and T. Bürgi, *J. Phys. Chem. C*, 2008, **112**, 5816–5824.
30 Z. Zhang, S. M. Zakeeruddin, B. C. O'Regan, R. Humphry-Baker and M. Grätzel, *J. Phys. Chem. B*, 2005, **109**, 21818–21824.
31 M. Zare, A. Mortezaali and A. Shafiekhani, *J. Phys. Chem. C*, 2016, **120**, 9017–9027.
32 B. M. Rabatic, N. M. Dimitrijevic, R. E. Cook, Z. V. Saponjic and T. Rajh, *Adv. Mater.*, 2006, **18**, 1033–1037.
33 J. U. Ha, J. Lee, M. A. Abbas, M. D. Lee, J. Lee and J. H. Bang, *ACS Appl. Mater. Interfaces*, 2019, **11**, 11391–11402.
34 W. Mönch, *Surf. Sci.*, 1983, **132**, 92–121.
35 M. Schmidt and S. G. Steinemann, *Fresenius. J. Anal. Chem.*, 1991, **341**, 412–415.
36 G. J. Fleming, K. Adib, J. A. Rodriguez, M. A. Barteau, J. M. White and H. Idriss, *Surf. Sci.*, 2008, **602**, 2029–2038.
37 L. Bertoluzzi, I. Herraiz-Cardona, R. Gottesman, A. Zaban and J. Bisquert, *J. Phys. Chem. Lett.*, 2014, **5**, 689–694.
38 H. Cachet and E. M. M. Sutter, *J. Phys. Chem. C*, 2015, **119**, 25548–25558.
39 H. Naseer, M. Jeon, H. Kim and J. H. Bang, *Surf. Interfaces*, 2025, **70**, 106827.
40 J. Bisquert, A. Zaban, M. Greenshtein and I. Mora-Seró, *J. Am. Chem. Soc.*, 2004, **126**, 13550–13559.
41 S. A. Kim, M. A. Abbas, L. Lee, B. Kang, H. Kim and J. H. Bang, *Phys. Chem. Chem. Phys.*, 2016, **18**, 30475–30483.
42 I. Mora-Seró and J. Bisquert, *Nano Lett.*, 2003, **3**, 945–949.
43 J. Bisquert, P. Cendula, L. Bertoluzzi and S. Gimenez, *J. Phys. Chem. Lett.*, 2014, **5**, 205–207.
44 G. Boschloo and A. Hagfeldt, *Acc. Chem. Res.*, 2009, **42**, 1819–1826.
45 Y. Wang, X.-H. Liu, Q. Wang, M. Quick, S. A. Kovalenko, Q.-Y. Chen, N. Koch and N. Pinna, *Angew. Chem., Int. Ed.*, 2020, **59**, 7748–7754.